Palaeogeography, Palaeoclimatology, Palaeoecology 337-338 (2012) 130–142

Contents lists available at SciVerse ScienceDirect

Palaeogeography, Palaeoclimatology, Palaeoecology

journal homepage: www.elsevier.com/locate/palaeo

Paleocene magneto-biostratigraphy and climate-controlled rock magnetism from the Belluno Basin, Tethys Ocean, Italy

Edoardo Dallanave [a,b,*], Claudia Agnini [a,c], Giovanni Muttoni [d,b], Domenico Rio [a]

[a] Department of Geosciences, University of Padova, Via G. Gradenigo 6, I-35131 Padova, Italy
[b] ALP – Alpine Laboratory of Paleomagnetism, Via Madonna dei Boschi 76, I-12016 Peveragno (CN), Italy
[c] IGG, CNR Padova, c/o Department of Geosciences, University of Padova, Via Gradenigo 6, I-35131 Padova, Italy
[d] Department of Earth Sciences, University of Milan, Via Mangiagalli 34, I-20133 Milano, Italy

ARTICLE INFO

Article history:
Received 13 October 2011
Received in revised form 3 April 2012
Accepted 8 April 2012
Available online 20 April 2012

Keywords:
Paleocene
Magnetostratigraphy
Calcareous nannofossils biostratigraphy
Rock-magnetic properties
Silicate weathering

ABSTRACT

The Paleocene South Ardo section consists of ~113 m of red to gray marls and calcareous marls continuously exposed along the South Ardo riverbed in the Venetian Southern Alps of Northern Italy. Magneto-biostratigraphic data imply that the section extends from magnetic polarity Chron C29r across the Cretaceous-Paleogene boundary to Chron C24r across the Paleocene–Eocene boundary, and from calcareous nannofossil *Micula murus* Zone in the Maastrichtian to Zone NP10 in the Ypresian. The average sediment accumulation rate, calculated by means of magnetic-polarity correlation with published Paleocene time scales, was found to vary from ~1.2 to 23 m/Myr throughout the section, and was used to calibrate the age of key calcareous nannofossil biohorizons, thus augmenting the resolution of existing time scales, as well as to migrate to the time domain the observed vertical variations of rock-magnetic properties. Our analyses allow to extend back into the Paleocene the temporal correlation between rock-magnetic properties and Earth's long-term climate previously observed in the neighboring late Paleocene–early Eocene Cicogna section. In detail, the composite South Ardo–Cicogna rock-magnetic dataset, which extends from ~65 Ma to 52.5 Ma, reveals that the warmer and more humid the climate, the higher the detrital hematite content of the sediments relative to maghemite/magnetite. We infer that our climate-controlled rock-magnetic curve reflects the efficiency of the silicate weathering mechanism to buffer pCO_2 long-term variations, and thus Earth's climate, during the Paleocene–Eocene.

1. Introduction

The Belluno Basin in the Venetian Southern Alps of Northern Italy (Fig. 1) hosts several continuous, expanded, and tectonically undisrupted stratigraphic sections spanning a ~30 Myr record of late Cretaceous to Eocene Tethyan marine sedimentation. The excellent paleomagnetic, paleontologic, and geochemical records of these sections have been used to improve the late Paleocene–Eocene time scale (Agnini et al., 2006; Dallanave et al., 2009; Agnini et al., 2011) as well as to shed light on Earth's climate variability from stable isotopes (Agnini et al., 2009; Spofforth et al., 2010) and rock-magnetic properties (Dallanave et al., 2010).

In this paper, we present the magnetic-polarity stratigraphy and rock-magnetism, integrated with the calcareous nannofossil biostratigraphy, of the ~113 m-thick upper Cretaceous–upper Paleocene South Ardo section, first described by Agnini et al. (2005) and Giusberti et al. (2007). The magneto-biostratigraphy of the section has been correlated to key deep-sea cores and land sections from the literature (e.g., Lowrie et al., 1982; Monechi and Thierstein, 1985; Agnini et al., 2006, 2007a, 2007b; Bowles, 2006; Dinarès-Turell et al., 2007) as well as to reference time scales (Cande and Kent, 1992, 1995 (CK95); Ogg and Smith, 2004 (GPTS04)), including the recent Paleocene astrochronological scale of Westerhold et al. (2008). These correlations allow to construct a preferred age model of sedimentation for migrating the biohorizons and the rock-magnetic data of the section from the depth to the time domain. We use the rock-magnetic dataset of the South Ardo section to verify the hypothesis put forward by Dallanave et al. (2010) for the Eocene of a strong control exerted by global climate variability on the type of detrital Fe-oxides deposited in the Belluno Basin; according to this hypothesis, the warm climate conditions of the PETM (Paleocene–Eocene thermal maximum) and of the early Eocene (Zachos et al., 2001) promoted the formation and deposition in the Belluno Basin of detrital hematite grains as by-products of silicate weathering processes active on land to buffer Earth's surface temperature variations (Walker et al., 1981; see also Kump et al., 2000). Our new data show that during the Paleocene, which is a time of relatively cooler climate conditions (Zachos et al., 2001), the sedimentation of detrital hematite

* Corresponding author at: Department of Earth and Environmental Sciences, Ludwig-Maximilians-Universität, Theresienstrasse 41, D-80333, Germany.
E-mail address: dallanave@geophysik.uni-muenchen.de (E. Dallanave).

0031-0182/$ – see front matter © 2012 Elsevier B.V. All rights reserved.
doi:10.1016/j.palaeo.2012.04.007

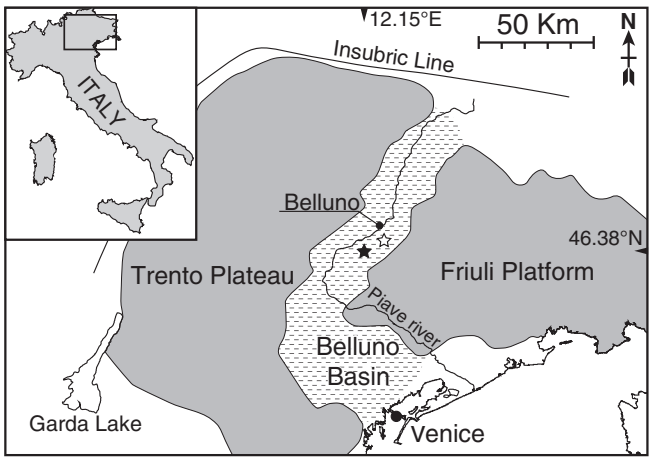

Fig. 1. Geological outline of the Belluno Basin in the Venetian Southern Alps of Italy, indicating the location of the South Ardo section (black star) (46.04°N, 12.15°E) and the Cicogna section (open star; Dallanave et al., 2009; 2010).

was inhibited, confirming that rock-magnetic properties can trace the efficiency of the silicate weathering negative feedback mechanism on both long (10^6 yr) and short (10^5 yr) time scales.

2. Geological setting

The Belluno Basin, which formed in the Early Jurassic between the Trento Plateau and the Friuli Platform (e.g., Winterer and Bosellini, 1981; Castellarin and Cantelli, 2000; Fig. 1), hosts Cretaceous to Eocene pelagic to hemipelagic successions consisting of 200–250 m of well-bedded, gray to red limestones and marly limestones pertaining to the Scaglia Rossa sensu lato (s.l.) (Di Napoli Alliata et al., 1970; Costa et al., 1996; Agnini et al., 2008).

The South Ardo section crops out ~12.6 km to the southwest of Belluno along the South Ardo creek at 46.38°N, 12.15°E, and consists of ~113 m of strata dipping to the NNW (~350°E) by ~15–20°. The Cretaceous–Paleogene (K/Pg) boundary, marked in the field by a ~1.5 cm-thick red "boundary clay" level containing phosphatic spheroids (Agnini et al., 2005), occurs in the lower part of the section (0 m level, Fig. 2). From the K/Pg boundary level up to ~14 m, the section consists of subnodular to well-stratified red marly limestones intercalated with 5 to 50 cm-thick white calcareous turbidites. From ~15 to 20 m, the sediments are organized in ~0.2–0.3 m-thick gray marly limestone–marl couplets, whereas from ~20 m upward, the sediments consist of gray to pale red marly limestones, with rare 1–5 cm-thick calcareous turbidites.

Previous low-resolution calcareous nannofossil biostratigraphy (Giusberti et al., 2007; Fornaciari E., unpublished data) suggests that the South Ardo section spans a complete Paleocene (Danian–Thanetian) record, from the K/Pg boundary to the early Eocene (Ypresian). In this part of the Belluno Basin, the Paleocene/Eocene boundary occurs at the base of a package of clays and marls thick up to ~3.5 m and referred to as Clay Marl Unit (CMU) (e.g., Giusberti et al., 2007; Dallanave et al., 2009); at South Ardo, where the stratigraphic interval containing the CMU does not crop out, the Paleocene/Eocene boundary can only be broadly placed between 101 and 106 m using nannofossil biostratigraphy (Fig. 2).

3. Material and methods

3.1. Calcareous nannofossils

Calcareous nannofossil analyses were carried out on 165 smear-slides, prepared using standard techniques, and studied using a

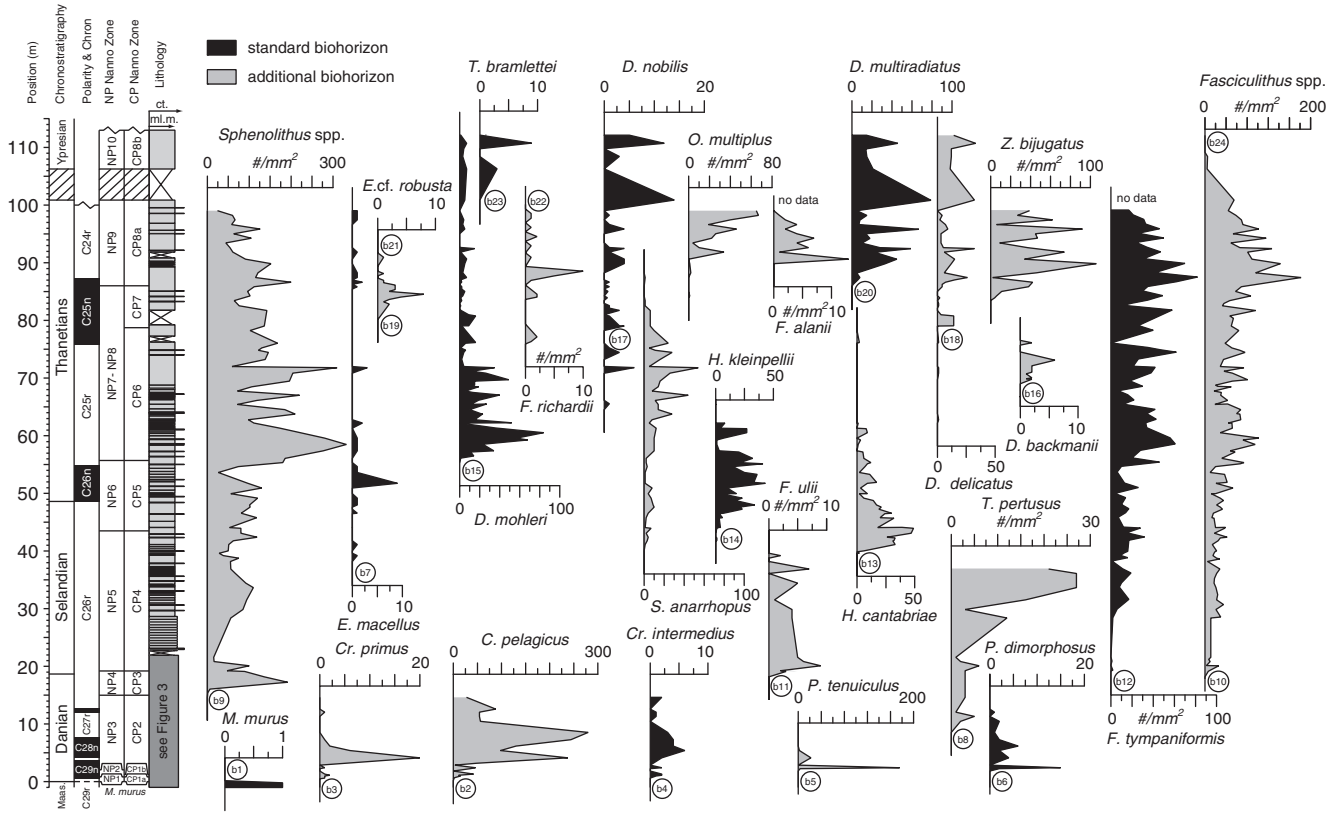

Fig. 2. Abundance patterns of selected nannofossil taxa from the South Ardo section are plotted against chronostratigraphy, magnetostratigraphy, calcareous nannofossils biostratigraphy, and lithostratigraphy (ml.m. = marly limestones and marls; ct. = calcareous turbidite levels). The K/Pg boundary is the 0 m level. For the lithologic details from −1 to 22 m, see Fig. 3. For description of biohorizons b1–b24, see text.

Zeiss Axioskop 40 light microscopy at a magnification of 1250. Samples were collected with an average spacing of ~1 m, except for intervals close to key biostratigraphic biohorizons, where samples were taken every ~20–40 cm.

The calcareous nannofossil biozonation for the Cretaceous interval is based on Romein (1979). The zonal schemes adopted for the Paleocene and early Eocene are those of Martini (1971, NP Zones) and Okada and Bukry (1980, CP Zones), modified following Fornaciari et al. (2007). The calcareous nannofossil biostratigraphy of the Danian interval has been revised several times (e.g., Romein, 1979; Perch-Nielsen, 1981; 1985a; Jiang and Gartner, 1986); the index species used in the standard zonations are often rare and discontinuous and, sometimes, difficult to determine because of taxonomic ambiguities. We adopted the emendation proposed by Fornaciari et al. (2007), using the LOs of *Cruciplacolithus intermedius*, *Chiasmolithus edwardsii*, *Prinsius dimorphosus*, and *Sphenolithus moriformis* gr. to mark the base of Zones NP2 (CP1b), CP2, NP3, and NP4 (CP3), respectively, integrated by some additional biohorizons such as the LOs of *Coccolithus pelagicus*, *Ericsonia cava*, *Prinsius tenuiculus* or *Toweius pertusus*. Zones NP7 and NP8 are not differentiated because *Heliolithus riedelii* is missing in the material studied. The taxonomy adopted in this work follows Perch-Nielsen (1985a, 1985b), with the exception of *Chiasmolithus* and *Cruciplacolithus* for which we adhere to Van Heck and Prins (1987) and Fornaciari et al. (2007).

Semiquantitative techniques were employed for counting selected calcareous nannofossil taxa to reconstruct their stratigraphic distribution patterns. The abundance of calcareous nannofossils was determined by counting the number of specimens in a prefixed area (N/mm^2) (Backman and Shackleton, 1983), except for very rare taxa for which three smear slide transects were counted (Fig. 2).

The calcareous nannofossil biohorizons have been defined using the abundance patterns of the index taxa following the rationale presented in Raffi et al. (2006). The bioevents used in this work are as follows: the Lowest Rare Occurrence (LRO), the Lowest Occurrence (LO), the Lowest Common Occurrence (LCO), the Highest Common Occurrence (HCO), the Highest Occurrence (HO), and the Acme Beginning (AB) (Table A1). In this paper, we use Lowest Occurrence (LO) and Highest Occurrence (HO) in preference to First Occurrence (FO) and Last Occurrence (LO) for reasons explained in Aubry (1995).

3.2. Paleomagnetic and rock-magnetic methods

Previous biostratigraphic data of Giusberti et al. (2007) were calibrated using calcareous nannofossil age estimates from Berggren et al. (1995) and used to derive preliminary sediment accumulation rates at South Ardo, which were estimated on the order of ~4 m/Myr for the basal ~20 m and ~17 m/Myr for the remainder of the section. Based on these estimates, we collected 158 core samples in the lower ~22 m of the section, with an average sampling interval of ~0.14 m, and 172 core samples from 28.4 m level up to ~100 m, with an average sampling interval of ~0.42 m (Fig. 3). The section in the 14.9–19.6 m and 21.6–28.4 m intervals is not accessible for core sampling as exposed along a vertical creek wall. All 330 core samples were collected with a gasoline-powered portable drill and oriented with a magnetic compass. Each core sample yielded a standard ~11 cm^3 oriented specimen for natural remanent magnetization (NRM) analysis. In addition, 281 weighted rock-chips were sliced from the oriented cores and used for rock-magnetic studies; paleomagnetic analyses were conducted at the Alpine Laboratory of Paleomagnetism (Peveragno, Italy).

The initial magnetic susceptibility of the 281 weighted rock-chip specimens was measured with an *AGICO KLY-3 Kappabridge*. The magnetic mineralogy of these specimens was determined by means of stepwise isothermal remanent magnetization (IRM) acquisition imparted with an *ASC Pulse Magnetizer* up to 2.5 T in 25 representative specimens; the IRM curves were then unmixed using the cumulative log-Gaussian (CLG) analyses of Kruiver et al. (2001). Eleven specimens from this suite were then subjected to thermal demagnetization of three orthogonal IRMs imparted in 2.5 T, 1.0 T, and 0.1 T inducing fields (Lowrie, 1990); the value of the IRM was measured after each of the 16 demagnetization steps from room temperature up to 670 °C with a *2G DC SQUID* cryogenic magnetometer placed in a magnetically shielded room. In order to evaluate the stratigraphic variations of the magnetic mineralogy across the section, the remaining 256 weighted rock-chip specimens were magnetized in 0.1 T and 1.0 T fields, and the value of the IRM was measured after each step; the $IRM_{1.0T}/IRM_{0.1T}$ ratio ($IRM_{1.0/0.1\,T}$) was then calculated and plotted versus stratigraphic depth.

To determine the magnetic-polarity sequence along the section, the 330 ~11 cm^3 oriented specimens were thermally demagnetized up to 680 °C in steps of 50 °C (or of 10–25 °C close to critical unblocking temperatures), and the component structure of the NRM was examined by means of vector end-point demagnetization diagrams (Zijderveld, 1967). We used the standard least-square analysis of Kirschvink (1980) on linear portions of the demagnetization paths to extract magnetic components, and the statistic analysis of Fisher (1953) to calculate the mean directions and the associated confidence parameters.

4. Calcareous nannofossil results

Calcareous nannofossil assemblages are usually rich and well diversified, and the preservation varies from poor to moderate, except for the Maastrichtian, where the heavy calcified forms *Micula* and *Watznaueria* dominate the assemblage, suggesting very poor preservation. The Danian is characterized by a marked improvement in preservation state as suggested by the common presence of small, more fragile placoliths. Middle to upper Paleocene assemblages are well preserved, showing a high diversity both in placoliths and nannoliths.

In the immediate aftermath of the K/Pg boundary, the nannofossil assemblages are dominated by thoracospherids and to a lesser extent by reworked specimens. A first important step in the calcareous nannofossil recovery is represented by the appearance of new genera, for instance *Coccolithus*, *Ericsonia*, *Cruciplacolithus*, and *Prinsius*, recorded at the Chron C29r/C29n transition (for magnetic polarity stratigraphy, see below). A second event of nannoplankton renewal is observed in the lower part of Chron C26r, where sphenoliths and fasciculiths first occur, and the genus *Toweius* increases its abundance becoming one of the dominant components of the assemblage. From then onward, the assemblages are mainly composed of common *Toweius* and *Coccolithus* in association with *Sphenolithus*, *Fasciculithus*, *Prinsius*, *Ericsonia*, and *Octolithus*. Several biostratigraphically useful taxa such as *Heliolithus*, *Discoaster*, *and Zygrhablithus* show their first occurrences during the middle–late Paleocene.

In detail, we recognized the following main calcareous nannofossil biohorizons (Fig. 2, Table A1).

- The discontinuous presence of *Micula murus* from the section base at −1 m up to the K/Pg boundary clay at 0 m indicates that this lowermost interval can be ascribed to the Maastrichtian *Micula murus* Zone (Bukry and Bramlette, 1970).
- The HO of *M. murus* (b1 in Fig. 2) and other Cretaceous taxa (the Cretaceous extinction plane), and the AB of *Thoracosphaera* and/or *Braarudosphaera bigelowii* are used to define the base of Zones NP1 (Martini, 1971) and CP1a, as defined by Romein (1979). These biohorizons co-occur at 0 m in correspondence with the K/Pg boundary.
- The LO of *C. intermedius* (*Cruciplacolithus tenuis auctt.*) is used to define the base of Zones NP2 and CP1b. At South Ardo, *C. intermedius* shows a rare but continuous presence from the lower part of Chron C29n at 0.84 ± 0.35 m (b4 in Fig. 2), after the LO of *Coccolithus pelagicus* and *Cruciplacolithus primus* (respectively b2 and b3 in Fig. 2; Table A1).

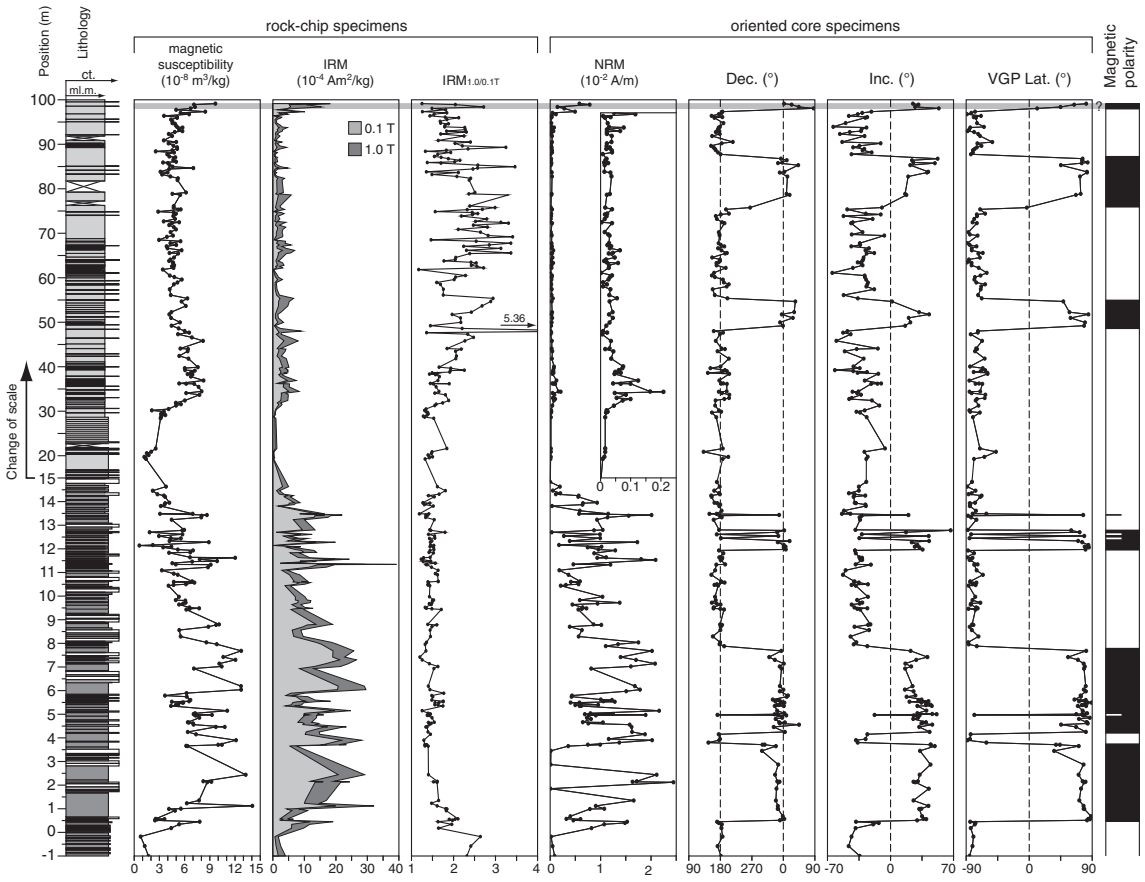

Fig. 3. Litho- and magnetostratigraphy of the South Ardo section (notice expanded vertical scale from −1 to 15 m). From left to right: lithology; initial magnetic susceptibility; isothermal remanent magnetizations (IRMs) (imparted at fields of 0.1 T and 1.0 T), and their ratio ($IRM_{1.0/0.1T}$); natural remanent magnetization (NRM; notice inset with expanded horizontal scale from 15 to 97.5 m); declination (Dec.) and inclination (Inc.) of the Ch magnetic directions and the associated virtual geomagnetic poles (VGP) latitude. The VGP latitudes were used to interpret the magnetic-polarity stratigraphy; black (white) bars represent normal (reverse) polarity intervals.

- The LO of *C. edwardsii*, used by Fornaciari et al. (2007) to subdivide Zone NP2 and mark the base of Zone CP2, occurs within Chron C29n at 1.24 ± 0.12 m (Table A1). The distinction between *C. edwardsii* and *C. asymmetricus* is difficult to perform in the overgrown assemblage of the studied section; therefore, the two species are merged together.
- The LO of *P. dimorphosus* marks the base of *Prinsius dimorphosus* Zone (Romein, 1979) and defines the base of NP3, as emended in Fornaciari et al. (2007). The common presence of small placoliths ascribed to *Prinsius tenuiculus* (b5 in Fig. 2) and *Prinsius dimorphosus* (b6 in Fig. 2) is found from 2.05 ± 0.2 m in the mid part of Chron C29n.
- The LO of *Ellipsolithus macellus* is used to define the base of Zones NP4 and CP3. In our material, *E. macellus* is absent in the Danian, becoming discontinuously present from the upper part of Chron C26r (b7 in Fig. 2), i.e. ~4 Myr after previous calibrations (e.g., Berggren et al., 1995). This uneven and delayed appearance prevents us from using *E. macellus* to define the base of Zone NP4 (or CP3), which can instead be placed using the lowest occurrence of sphenoliths (see below).
- The LO of *T. pertusus*, a possible additional biohorizon, has been observed at 9.52 ± 0.96 m within C27r (b8 in Fig. 2).
- The LO of *Sphenolithus moriformis* gr., which includes all sphenoliths with a dome shape structure (Perch-Nielsen, 1985a), is here used to define the base of Zone NP4 (CP3). In the South Ardo section, sphenoliths show a common and continuous presence since their very first entry within Chron C26r at 15.02 ± 0.39 m (b9 in Fig. 2).
- The LO of *F. tympaniformis* marks the base of Zone NP5 (CP4). The LO of *F. ulii* is an alternative biohorizon to place the base of Zone NP5 (CP4). At South Ardo, the LOs of *Fasciculithus* spp. and of *F. ulii* occur in the lower part of Chron 26r at 18.68 ± 0.47 m (respectively b10 and b11 in Fig. 2), while the LO of *F. tympaniformis* lies at 19.20 ± 0.06 m still in the lower part of Chron 26r (b12 in Fig. 2).
- The LO of *Heliolithus cantabriae* slightly predates the LO of *H. kleinpellii* and represents a useful event occurring at 39.97 ± 0.08 m in the upper part of Chron C26r (b13 in Fig. 2).
- The LO of *Heliolithus kleinpellii* defines the base of Zone NP6 (CP5). At South Ardo, this biohorizon lies in the upper part of Chron C26r at 43.54 ± 0.42 m (b14 in Fig. 2).
- The LO of *Discoaster mohleri*, which defines the base of Zone NP7 (CP6), has its first appearance at 55.74 ± 0.38 m at the base of Chron C25r (b15 in Fig. 2).
- The LO of *Discoaster backmanii* occurs at 68.14 ± 0.38 m in the upper third of Chron C25r (b16 in Fig. 2).
- The LO of *Discoaster nobilis* is used to define the base of Zone CP7. This biohorizon is difficult to place precisely at South Ardo because *D. nobilis* is initially rare and discontinuous, becoming more abundant and continuous from 78.66 ± 0.40 m, where the base of CP7 is placed (b17 in Fig. 2).
- The LO of *Discoaster delicatus* occurs at 79.08 ± 0.02 m within Chron C25n (b18 in Fig. 2), and is used to approximate the base of Zone CP7 at South Ardo, where *Discoaster nobilis* shows a discontinuous distribution (see above).
- The LO of *Discoaster multiradiatus*, which marks the base of Zone NP9a (and CP8a), occurs in the upper part of Chron C25n at 86.06 ± 0.20 m (b20 in Fig. 2).
- The LO and HO of *Ericsonia* cf. *robusta* are observed within Chron C25n at 80.41 ± 1.35 and 90.26 ± 0.40 m, respectively (b19 and

b21 in Fig. 2). *E.* cf. *robusta* shows a short stratigraphic range straddling the LO of *D. multiradiatus* (Raffi et al., 2005; Agnini et al., 2007a; Dallanave et al., 2009).

The South Ardo section does not crop out from 100.9 to 106.3 m level; the Paleocene–Eocene transition is placed within this 5.4 m-thick interval according to paleontologic data from correlative sections of the Belluno Basin (Agnini et al., 2007b; Dallanave et al., 2009). The HOs of heavily calcified *Fasciculithus* species such as *F. richardii* (b22 in Fig. 2) as well as the LO of *T. bramlettei* (b23 in Fig. 2), which marks the base of Zone NP10, presumably fall somewhere in this stratigraphic interval, since the final extinction of the former taxon has been observed within Chron C24r at 108.82 ± 0.38 m (b24 in Fig. 2) while a few specimens of the latter taxon were found at 106.3 m. Furthermore, the LO of the genus *Rhomboaster*, which defines the base of Zone CP8b and is stratigraphically restricted to the PETM, is not observed at South Ardo.

Other additional or alternative biohorizons not described in this paragraph, but considered to be useful or at least promising for biostratigraphic aims, are reported in Table A1 and Fig. 2.

5. Rock magnetism

5.1. Initial magnetic susceptibility (IMS)

The IMS generally varies between 0.6 and 14.1×10^{-8} m^3 kg^{-1} (Fig. 3). The basal meter of the section, below the K/Pg boundary, is characterized by low values (~$1–2\times10^{-8}$ m^3 kg^{-1}). From 0 to 2.5 m, the IMS rises to a peak value of 14.1×10^{-8} m^3 kg^{-1}; from 2.5 to ~9 m, it maintains relatively high – albeit variable – values due to the presence of largely diamagnetic carbonate turbidites. From ~9 to 15 m, the IMS shows a smooth decrease and maintains generally low values up to 30 m, followed by an increase between ~30 and ~35 m. From there up to the top of the section, the IMS varies between 2 and 8×10^{-8} m^3 kg^{-1}.

5.2. IRM acquisition and thermal decay

The CLG analysis (Kruiver et al., 2001) of the IRM acquisition curves reveals the presence of two distinct magnetic coercivity phases (Fig. 4A) in all specimens: a low magnetic coercivity (LMC) phase characterized by a mean $B_{½}$ value (the field at which half of the saturation magnetization is reached) of 48.6 mT, and a high magnetic coercivity (HMC) phase characterized by a mean $B_{½}$ of 482 mT. From section base to top, the key features of these magnetic coercivity phases are as follows:

Specimen ar002 (0.6 m below the K/Pg boundary; Fig. 4) is dominated by the HMC phase, which contributes for ~72% to the saturation IRM (SIRM), coexisting with the LMC phase, which contributes for ~28% to the SIRM. The HMC phase consists of hematite, as revealed by the thermal demagnetization of the three-component IRM (IRM_{TD}), which is characterized by the presence of 2.5 T and 1.0 T magnetic phases with maximum unblocking temperature of 670 °C (Fig. 4B). The LMC phase consists of maghemite, as revealed by the 0.1 T coercivity phase approaching zero intensity values at ~625 °C; maghemite is in fact typically characterized by low coercivity and a Curie temperature comprised between 590 and 675 °C (Tauxe, 2010). Between 0 m and ~15 m, the CLG and the IRM_{TD} diagrams reveal a similar hematite and maghemite mixture, but with the LMC maghemite phase dominating the IRM (~80% of the SIRM; Fig. 4, ar024).

From ~15 to 30 m, the IRM spectra are largely dominated by the LMC phase, which contributes to the SIRM for more than 90% (Fig. 4, ar070). The associated IRM_{TD} diagram is dominated by the 0.1 T coercivity phase, followed by the 1.0 T phase, both approaching zero intensity at ~600 °C. Both the 0.1 and 1.0 T phases are interpreted as maghemite and/or magnetite; this is because the LMC fraction tends to saturate at ~0.3 T (i.e., ~2.5 on the logarithmic scale of the linear acquisition plot in Fig. 4A) and is consequently not completely picked up by the 0.1 T IRM_{TD} axis. The 2.5 T coercivity phase is virtually absent.

From ~30 m up to the section top, the HMC hematitic phase, which possesses maximum unblocking temperature of 670 °C, dominates the coercivity spectra of the specimens, contributing for 65–70% to the SIRM. This HMC phase coexists with a LMC phase (30–35% of the SIRM), which likely consists of maghemite and/or magnetite, as revealed by the 0.1 T coercivity phase approaching zero intensity at 550–625 °C (Fig. 4; e.g., specimens ar120, ar162).

5.3. $IRM_{0.1T}$, $IRM_{1.0T}$, and $IRM_{1.0/0.1T}$

The $IRM_{0.1T}$ and $IRM_{1.0T}$ can be used to evaluate in detail the stratigraphic variability of the LMC and the HMC phases throughout the section. They both display low values in the basal meter of the section, rising in the ensuing ~2 m to mean values of ~9 ($IRM_{0.1T}$) and ~13 ($IRM_{1.0T}$) $\times10^{-4}$ Am^2 kg^{-1}, which are maintained up to ~9 m. They show a decreasing trend from ~9 to 15 m to then maintain relatively low values upsection ($IRM_{0.1T}$ = ~1.5×10^{-4} Am^2 kg^{-1}; $IRM_{1.0T}$ = ~3×10^{-4} Am^2 kg^{-1}), followed in the uppermost ~3 m by a marked positive swing (Fig. 3).

We evaluated the relative variations of the HMC vs LMC phases along the section, and thus the relative variations of the hematite content with respect to maghemite/magnetite, by means of the $IRM_{1.0/0.1T}$ ratio. Theoretically, this ratio starts from 1, when only low coercivity magnetite/maghemite are present, to progressively increase when the relative contribution of high coercivity hematite increases; therefore, the higher (lower) the ratio, the higher (lower) the hematite content relative to magnetite/maghemite. $IRM_{1.0/0.1T}$ values are generally low throughout the section, being less than 2 in the lower ~40 m of the section to slightly increase up to ~3 in the reminder of the section; a single horizon at 48 m yielded $IRM_{1.0/0.1T}$ values of ~5. These generally low values indicate overall small hematite contents relative to dominant maghemite/magnetite, with the possible exception of the horizon at 48 m associated with a brief rising of hematite abundance.

6. Paleomagnetism

6.1. Paleomagnetic directions and poles

The intensity of the NRM of the 330 oriented core samples ranges between 2×10^{-3} and 2.45×10^{-2} A/m in the 0–15 m of section; lower values are observed in upper Cretaceous sediments (from −1 m to 0 m) as well as in correspondence of carbonatic turbidites (e.g., at 1.85, 2.87, and 3.45 m) (Fig. 3). A marked decrease of NRM intensity is observed at ~13–15 m, where the sediments gradually turn from red to gray color. From ~15 m up to 97 m, the NRM ranges between 1×10^{-3} and 0.78×10^{-2} A/m with a marked swing toward higher values between 97 and 100 m.

Scattered magnetic A component directions statistically oriented N-and-down in geographic (in situ) coordinates are commonly observed from room temperature up to 200–300 °C (Fig. 5A, B). In 68 samples from 0 to 14 m as well as in 3 samples from the uppermost meter of the sampled section, this A component is followed by a more stable B component oriented N-and-down that can reach maximum unblocking temperatures of ~550 °C (Fig. 5A, e.g., samples ar005, ar012, ar048, and ar223; Fig. 5B). This average B direction is

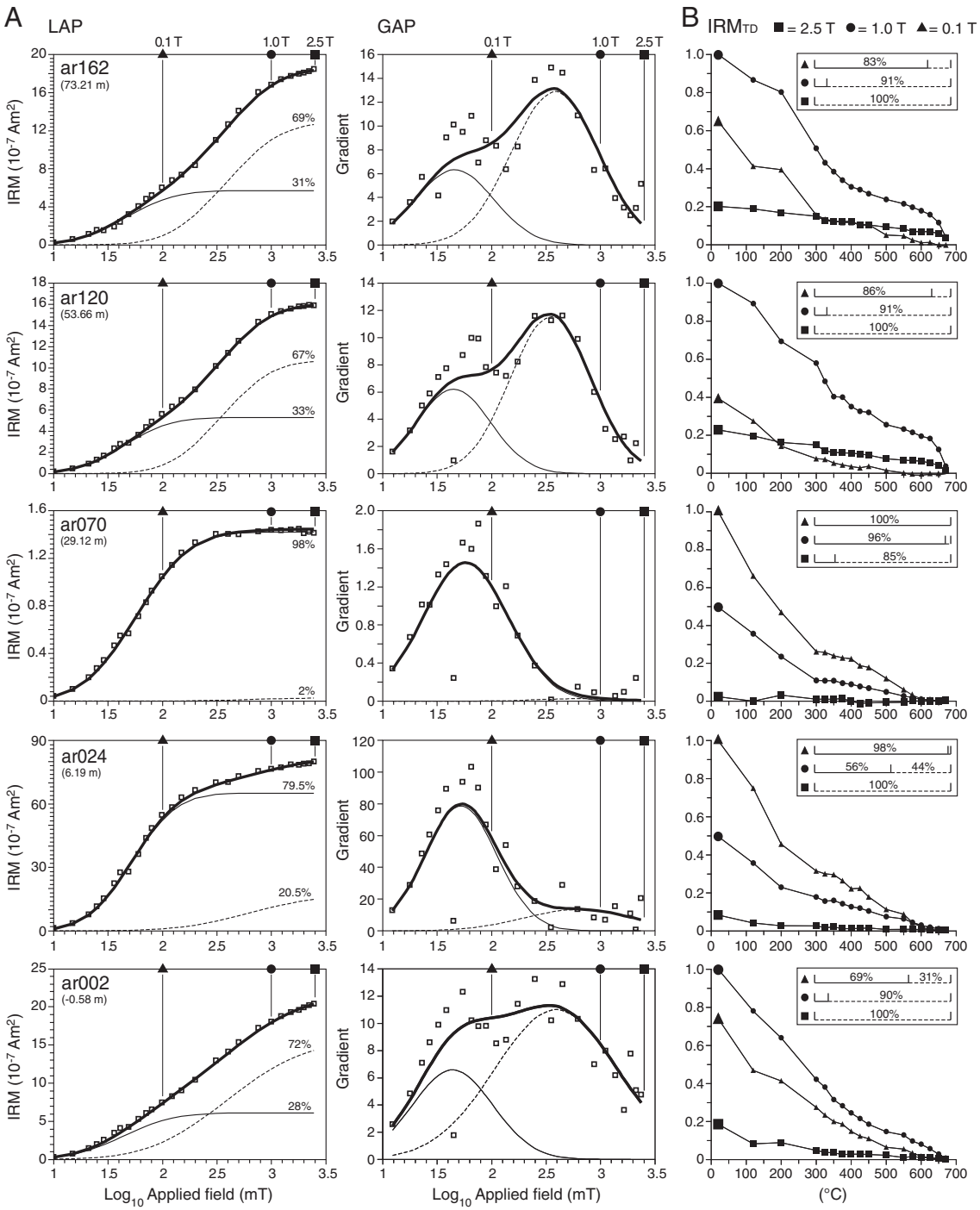

Fig. 4. (A) Cumulative log-Gaussian analyses of the IRM stepwise acquisition curves of six representative specimens with indication of the stratigraphic position; LAP = linear acquisition plot; GAP = gradient acquisition plot. The open squares represent IRM data. The thin solid and dashed lines represent, respectively, the low magnetic coercivity (LMC) component and the high magnetic coercivity (HMC) component; the % contribution of each component to the saturation IRM (100%) is also indicated; the thick solid line represents the sum of the two components. The closed triangle, circle, and square on the upper horizontal axis of each plot represent the location on the $\log_{10}$ Applied field axis of the 0.1 T, 1.0 T, and 2.5 T inducing fields used for the thermal demagnetization of the three-component IRM. (B) Thermal demagnetization of the three-component IRM (IRM_{TD}; Lowrie, 1990) of the specimens illustrated in panel (A); squares, circles and triangles represent the thermal demagnetization along the 2.5 T, 1.0 T, and 0.1 T axes, respectively. The insets represent the % value of the LMC (solid line) and of the HMC (dashed line) picked up by the 2.5 T, 1.0 T, and 0.1 T axes as calculated by the CLG diagrams in panel (A).

statistically undistinguishable from the characteristic (Ch) normal polarity mean direction (described below) at the 95% level of confidence (inset in Fig. 5B), as revealed by the procedure of Watson (1983) ($V_w = 3.8$; $V_{critical} = 6.1$; see also Tauxe, 2010), and is generally interpreted as a thermochemical overprint possibly associated with the Cenozoic Alpine orogeny. Finally, Ch directions linearly trending to the origin of the vector end-point diagrams axes have been isolated in 241 core samples (73% of the total) up to maximum unblocking temperatures of 625–670 °C. These Ch directions are organized in two clusters oriented N-and-down or S-and-up in geographic (in situ) coordinates, and they become somewhat shallower after correction for bedding tilt (Fig. 5C). The mean Ch directions depart from antipodality by 2.3° and pass the Watson (1983) reversal test at the 95% level of confidence ($V_w = 1.5$; $V_{critical} = 5.9$), corresponding to a

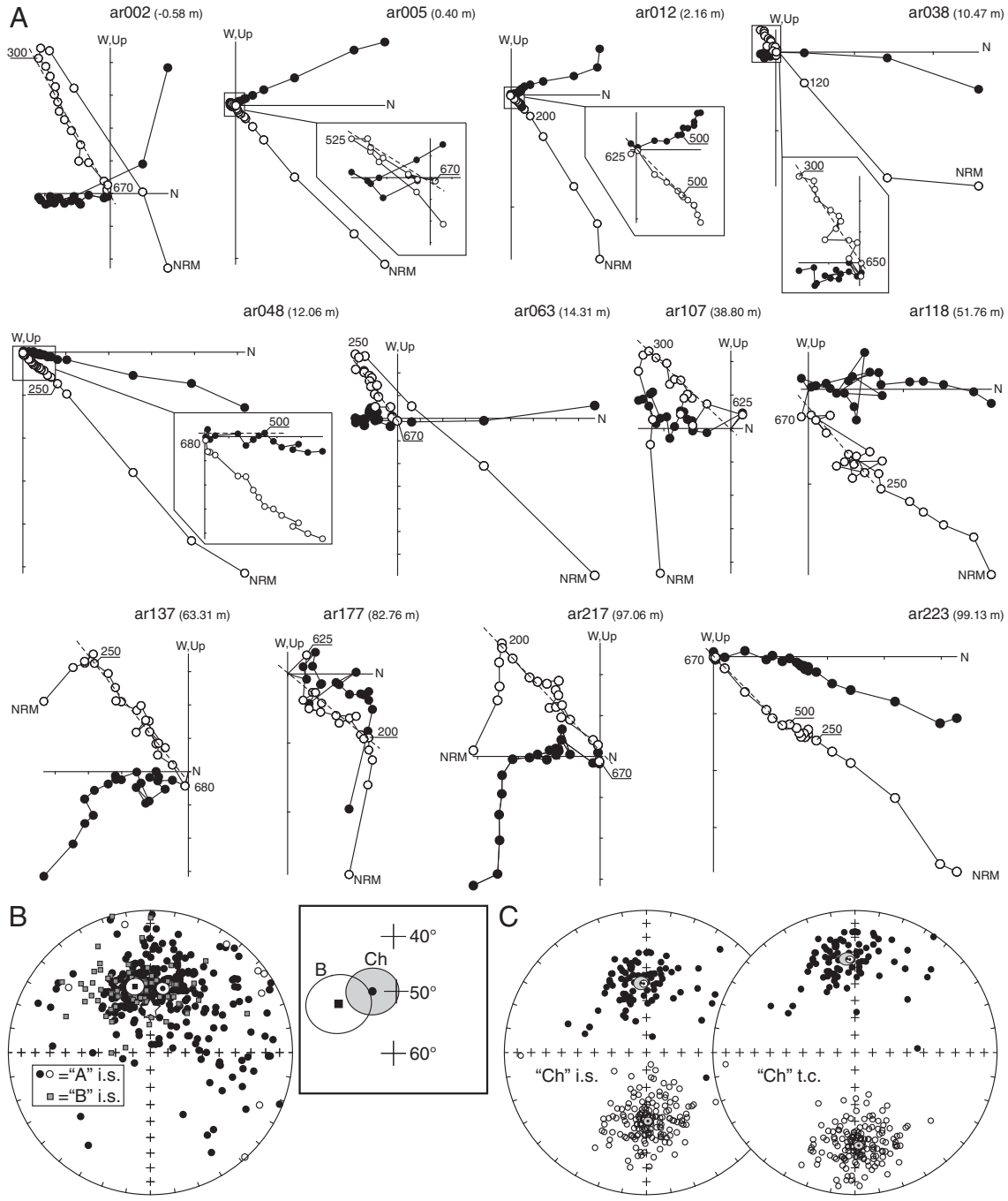

Fig. 5. (A) Vector end-point demagnetization diagrams of the NRM of representative oriented core samples from the South Ardo section, with indication of the stratigraphic position. Closed (open) circles are the projections onto the horizontal (vertical) plane in "in situ" coordinates. (B) Equal area projections of the A and B component directions of the NRM (i.s. = "in situ" coordinates); closed (open) symbols represent down-pointing (up-pointing) directions. The white circles and the white star represent, respectively, the α95 cones of confidence of the mean directions (Fisher, 1953), and the present day geomagnetic field direction calculated using the geocentric axial dipole (GAD; Bulter, 1998) field model. The inset shows the B and the normal polarity Ch mean directions (closed square and circle, respectively) with the associated α95 cones of confidence. (C) Equal area projections of the Ch component directions of the NRM (t.c. = tilt corrected coordinates); the gray circles represent the α95 cones of confidence associated with the two clusters of N-and-down and S-and-up mean directions, while the white circles represent the α95 cones of confidence associated with the mean directions after inverting all the Ch components to a common normal polarity.

reversal test of class "A" of McFadden and McElhinny (1990). Inverting all directions to a common normal polarity, we obtained a tilt corrected mean direction of Dec. = 356.8°, Inc. = 34.7° (N = 241, k = 19.9, α95 = 2.1°) (Table 1).

We calculated the position of the virtual geomagnetic pole (VGP) for each Ch direction in order to outline magnetic-polarity stratigraphy (Fig. 3). A selection of 139 VGPs from Ch directions with maximum angular deviation (MAD) lower than 10° was used to determine the mean paleomagnetic pole of the section at Long. = 204.0°E, Lat. = 63.0°N (K = 26.8, A95 = 2.4°) (Fig. 6A and Table 1, pole 'South Ardo 1'). We compared the Paleocene (65–55 Ma) South Ardo 1 paleomagnetic pole to the late Cretaceous–early Oligocene master apparent polar wander path (APWP) for Africa of Besse and Courtillot (2002, 2003) (hereafter referred to as BC03), and found that it is removed from the 60 Ma paleomagnetic poles of Africa by ~13° in the far side direction relative to the sampling site (Fig. 6A). This deviation is the consequence of an inclination shallowing of the mean Ch direction of ~18° with respect to the direction expected at South Ardo from the African APWP (Fig. 6B).

Table 1
Characteristic component directions and paleomagnetic poles of the South Ardo section.

N	MAD	Geographic (in situ) coordinates				Bedding (tilt-corrected) coordinates				
		k	α_{95}	DEC	INC	*k*	α_{95}	DEC	INC	INC*
Normal polarity directions										
83	8.1 ± 4.9	16.3	4.0	355.5	49.4	16.0	4.0	355.1	34.2	–
Reverse polarity directions										
157	12.9 ± 7.3	22.2	2.4	178.8	−50.1	22.8	2.4	177.7	−35.0	–
Reverse and normal polarity directions										
240	11.3 ± 6.9	19.8	2.1	357.7	49.9	19.9	2.1	356.8	34.7	$51.7^{61.4}_{41.5}$

Paleomagnetic pole South Ardo 1					Paleomagnetic pole South Ardo 2	
N	K	A_{95}	LONG	LAT	LONG	LAT
139	26.8	2.4	204.0	63.0	211.9	75.6

N = number of samples; MAD = mean angular deviation of the mean paleomagnetic direction expressed in degrees; k and K = Fisher precision parameters of the mean paleomagnetic direction and pole, respectively; α_{95} and A_{95} = Fisher radius of cone of 95% confidence associated with the mean paleomagnetic direction and pole, respectively; DEC and INC = declination and inclination of the mean paleomagnetic direction; INC* = inclination of the mean paleomagnetic direction corrected for inclination shallowing; LONG and LAT = longitude of the mean paleomagnetic pole before (South Ardo 1) and after (South Ardo 2) correction for inclination shallowing.

The unblocking temperatures of the Ch directions and the rock-magnetic analyses suggest that the magnetization is carried mainly by hematite, and it is well known that shallow bias magnetic directions may be associated with detrital hematite (Tauxe and Kent, 1984). We detected and corrected for the inclination flattening using the elongation/inclination (E/I) statistical method of Tauxe and Kent (2004; see also Kent and Tauxe, 2005; Tauxe et al., 2008); we progressively "unflattened" the selected 139 Ch directions by decreasing the flattening parameter "*f*" (King, 1955) within the formula $\tan I_f = f \cdot \tan I_0$ (where I_f and I_0 are the measured inclination and the true inclination of the magnetic field during sedimentation, respectively) so that the directional dataset assumed an E/I pair of values consistent with the TK03.GAD field model (Tauxe and Kent, 2004; Tauxe, 2005; Tauxe et al., 2008). To evaluate the uncertainty of this estimate, we repeated the analyses by generating 5000 bootstrapped datasets, obtaining a mean value of f = 0.5 and an unflattened mean characteristic inclination of Inc. = $51.7^{\circ}{}^{61.4^{\circ}}_{41.5^{\circ}}$ (Fig. 6C, D), which is now in agreement with the expected inclination at South Ardo calculated from the reference 60 Ma paleomagnetic poles of Africa (Inc. = 51.8); accordingly, the unflattened South Ardo 2 pole falls on the 60–50 Ma African APWP, rotated by a statistically insignificant angle of 2.4° clockwise with respect to the 60 Ma African paleopole (Fig. 6).

6.2. Magnetic-polarity stratigraphy

The latitude of each core sample VGP relative to the mean paleomagnetic (north) pole axis was used for interpreting polarity stratigraphy (Lowrie and Alvarez, 1977; Kent et al., 1995). Relative VGP latitudes approaching 90°N (90°S) are interpreted as recording normal (reverse) polarity. These data (Fig. 3) show a ~1.5 m thick reverse polarity interval at the section base, straddling the K/Pg boundary, followed by ~7.3 m of dominantly normal polarity, embedding a ~0.5 m reverse polarity interval across the 4 m level. Up section, magnetic polarity is dominantly reverse, with the presence of three main normal polarity intervals at 11.95–12.79 m, 48.61–55.01 m, and 75.76–87.26 m. The uppermost meter of the sampled section is also characterized by normal polarity, which however correlates with peak values of IMS, IRMs, and NRM and is tentatively regarded as a chemical overprint, and therefore excluded from magnetic polarity interpretation.

We compared the South Ardo magneto-biostratigraphy with data from correlative key sections from the literature, namely Zumaia from northern Spain (Dinarès-Turell et al., 2002, 2003, 2007), ODP Site 1262 from the Walvis Ridge (Bowles, 2006; Agnini et al., 2007a; Westerhold et al., 2008), and the classic Contessa Highway section from the central Appennines near Gubbio, Italy (Lowrie et al., 1982;

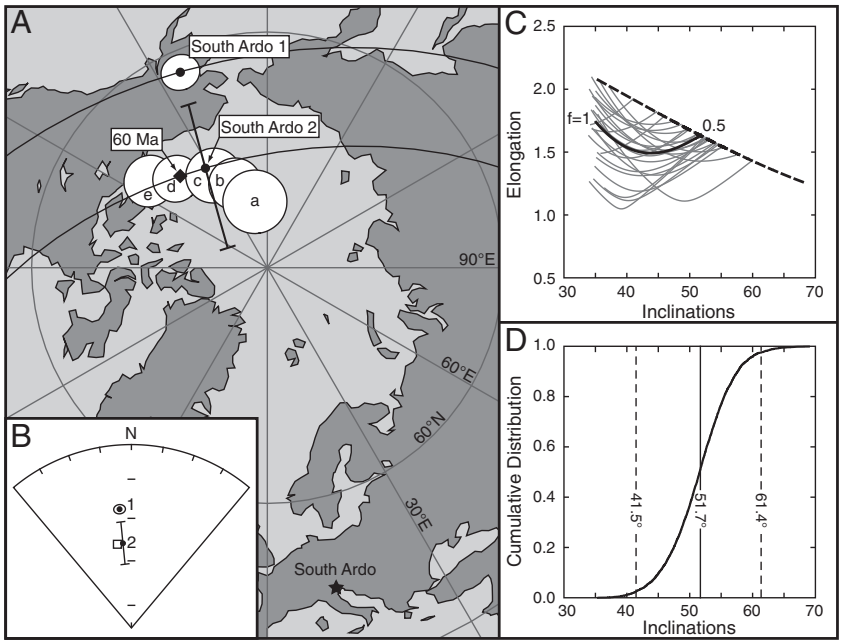

Fig. 6. (A) The mean paleomagnetic pole from the South Ardo section before (South Ardo 1) and after (South Ardo 2) correction for the inclination flattening is compared to the master apparent polar wander path (APWP) of Africa for the 30–70 Ma interval (a–e circles) (Besse and Courtillot, 2003; BC03); the closed diamond represents the estimated position of the reference 60 Ma African pole (map drawn with PaleoMac; Cogné, 2003). Panel (B) shows the characteristic mean direction from South Ardo before (1) and after (2) directional unflattening, with the associated 95% confidence boundaries; these mean directions are compared to the mean direction expected at South Ardo from the reference 60 Ma paleopole for Africa (open square). (C) The E/I values of the systematically unflattened directions with the flattening factor f ranging from 1 to 0.5 (heavy line) are compared to the E/I values predicted by the TK03.GAD geomagnetic field model (dashed line); 25 of 5000 bootstrapped data set are shown by the light lines. (D) Diagram of the cumulative distribution of all inclinations derived from the bootstrapped crossing points, with the associated 95% confidence boundaries (41.5°–61.4°) around the mean value (51.7°).

Monechi and Thierstein, 1985). All sections show excellent magnetic-polarity correlations supported by standard calcareous nannofossil biohorizons that show high consistency in their relative ranking and spacing between sections (Fig. 7). When correlated to the CK95 time scale, the 11 polarity intervals of the South Ardo section are found to straddle from Chron C29r to C24r in the ~65 to 55.5 Ma interval (Fig. 7).

7. Age model of sedimentation and biochronology

We constructed an age-depth plot for the South Ardo section (Fig. 8) by means of magnetic-polarity correlation with the reference CK95 time scale as well as the time scale of Ogg and Smith (2004; GPTS04) and the two options for the Paleocene proposed by Westerhold et al. (2008) obtained by the astronomical calibration of various deep-sea cores and outcropping sections. We used as chronologic control points the 10 magnetic reversals retrieved in the section, straddling between the top of Chron C29r and the base of Chron C24r, as well as the K/Pg boundary. For each correlation option, we derived a sediment accumulation rate curve, which we assumed constant between each pair of the 11 tie points (Fig. 8, Table A2). The obtained age models imply sediment accumulation rates of ~1–5 m/Myr between the K/Pg boundary and C27n(0.0) (i.e. between 0 and 12.8 m), followed upsection by a progressive increase of sedimentation rates from ~12 to 20–24 m/Myr (Fig. 8).

The CK95- and GPTS04-based age models have been used to estimate the ages of standard as well as additional key calcareous nannofossil biohorizons at South Ardo (Table A1), which have been found to be consistent with the ages of correlative biohorizons from sections within the Belluno Basin (e.g., Cicogna) as well as from sections located elsewhere in the Tethys (i.e., Contessa Highway) and outside of the Tethys (i.e., ODP Site 1262, Zumaia), suggesting that low latitudinal temperature gradients during the Paleocene and early Eocene may have favored a wider paleobiogeographic distribution of calcareous nannofossils.

The ~400 kyr time interval between the base of Chron C25n and the base of Chron C24r is characterized by a remarkable concentration of bioevents defining a phase of prominent modification of calcareous nannofossil assemblages, particularly within the nannoliths. The observed biotic changes seem to be coeval with the B1 and B2 negative $\delta^{13}C$ shifts described by Cramer et al. (2003) within C25n at various DSDP and ODP sites.

8. Climate control on the Fe-oxides sedimentation

The new rock-magnetic dataset from the South Ardo section allows us to extend back to the basal Paleocene the model of climate

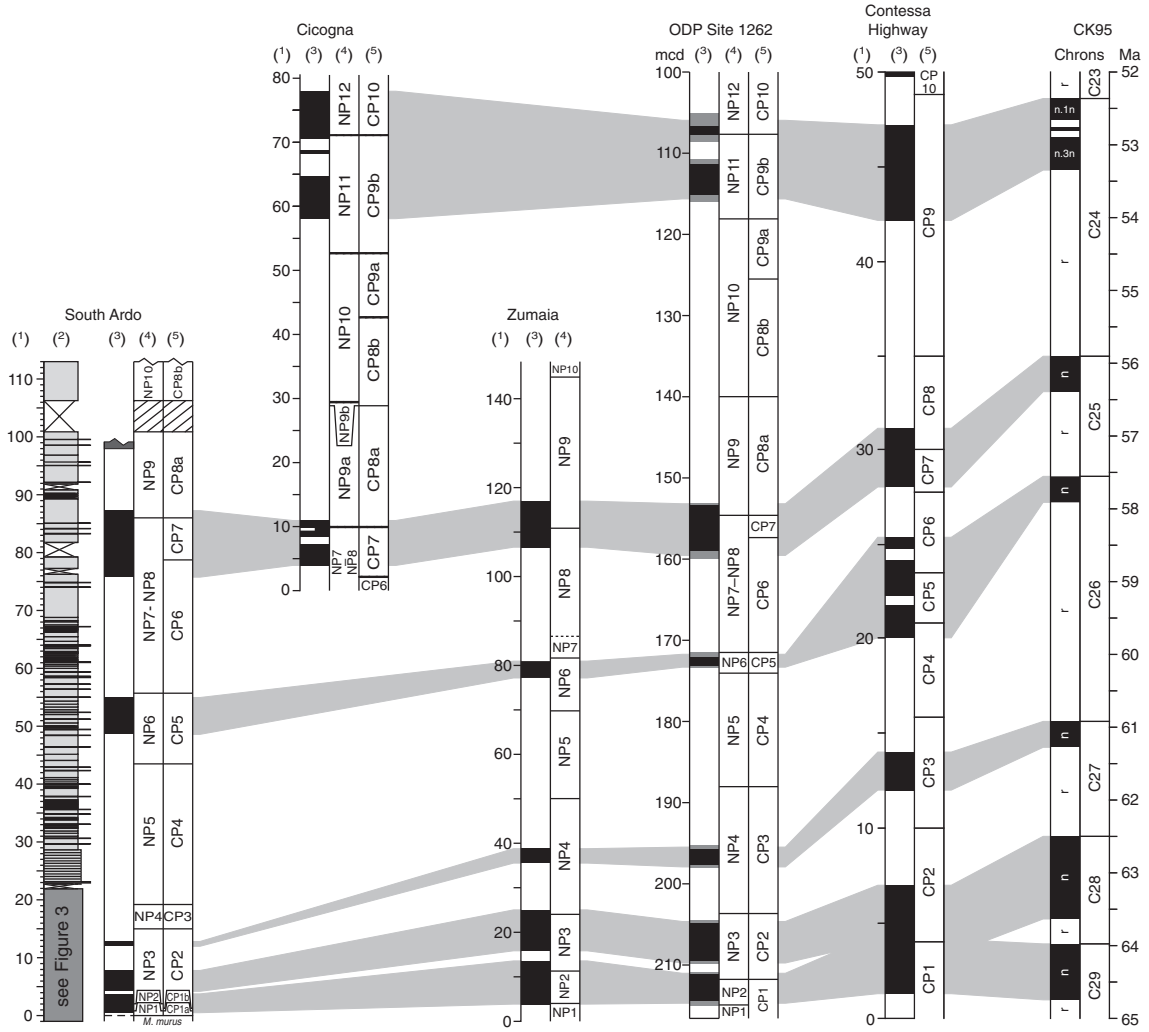

Fig. 7. The magneto-biostratigraphy of the South Ardo section is correlated to magneto-biostratigraphies from the Basque Basin in Spain (Zumaia), Walvis Ridge in the SE Atlantic (ODP Site 1262), and Umbria–Marche in central Italy (Contessa Highway), as well as to the CK95 geomagnetic polarity time scale (Cande and Kent, 1995); Notes: (1) = stratigraphic depth (m); (2) = lithology (see text and Fig. 2 for details); (3) = magnetic polarity; (4) = NP Calcareous nannofossil biozonation (Martini, 1971); (5) = CP Calcareous nannofossil biozonation (Okada and Bukry, 1980); mcd = meters composite depth.

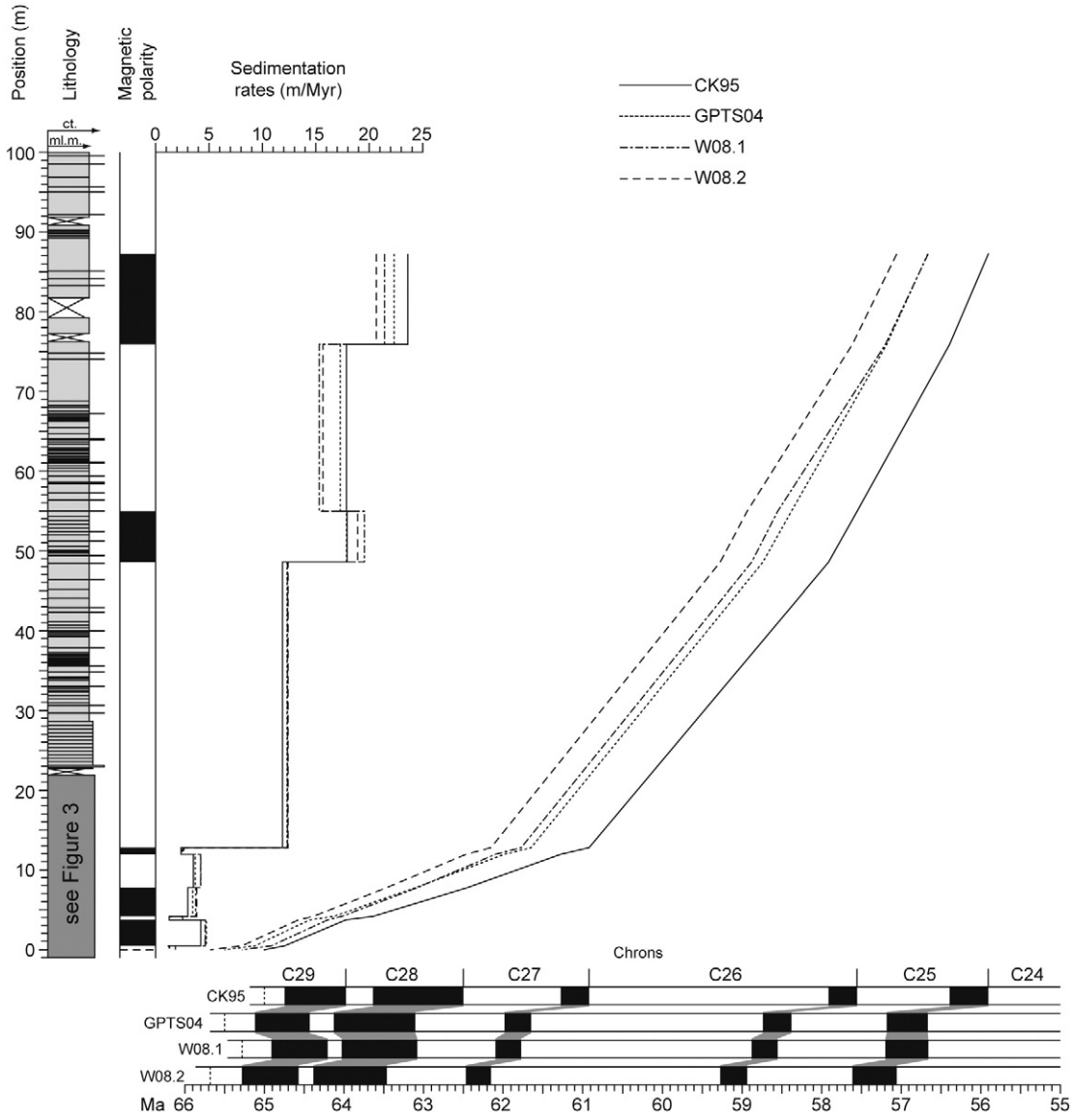

Fig. 8. Age-depth models and derived sediment accumulation rates for the South Ardo section obtained by magnetostratigraphic correlation to the geomagnetic polarity time scale of Cande and Kent (1995; CK95), Ogg and Smith (2004; GPTS04), and the two time tuning options for the Paleocene proposed by Westerhold et al. (2008; W08.1 and W08.2).

forcing on sedimentation proposed by Dallanave et al. (2010). These authors studied the rock-magnetic properties of the late Paleocene–early Eocene Cicogna section and found evidences of a climatic control on type of Fe-oxides deposited as detrital phases in the Belluno Basin. In particular, they described a relative increase of detrital hematite during both short-term and long-term warming periods (PETM and early Eocene, respectively) as revealed by a statistical correlation between the $IRM_{1.0/0.1T}$ record and the benthic $\delta^{18}O$ record of Zachos et al. (2001).

Following this idea, we migrated to the time domain the $IRM_{1.0/0.1T}$ record of the South Ardo section by using the CK95-based age model, and integrated it with the $IRM_{1.0/0.1T}$ record from Cicogna (Dallanave et al., 2010). We then compared the composite Paleocene-early Eocene South Ardo–Cicogna $IRM_{1.0/0.1T}$ record to the coeval (CK95-calibrated) $\delta^{18}O$ record of Zachos et al. (2001) (Fig. 9). As expected, from 65 Ma (K/Pg boundary) up to ~55.5 Ma across a Paleocene interval of relatively high $\delta^{18}O$ values (relatively cool climate), the $IRM_{1.0/0.1T}$ ratio is relatively low, suggesting relatively scarce hematite of detrital origin (as it carries a Ch component affected by inclination shallowing; see above). This long-term trend is punctuated by an abrupt and transient increase at the C26r/C26n transition (0.44 Ma after the LO of *H. kleinpellii*). This very short-lived $IRM_{1.0/0.1T}$ rising is coeval with an increase in the magnetic susceptibility reported from the Equatorial Pacific (Westerhold and Röhl, 2006) and associated to the early late Paleocene Event (ELPE), a brief warming event recently reported by different authors (Zachos et al., 2004; Petrizzo, 2005; Bernaola et al., 2007). From the Paleocene–Eocene boundary upsection, across the PETM and during the early Eocene, the $IRM_{1.0/0.1T}$ ratio shows positive swings up to values of ~7 (Dallanave et al., 2010), indicative of relatively more abundant detrital hematite contents.

This temporal coupling between climate and Fe-oxide formation is in agreement with weathering processes observed in recent and subrecent soils. Torrent et al. (2006) demonstrated that under continental aerobic conditions, the weathering oxidation process of Fe-bearing primary minerals is typified by the ferrihydrite → maghemite → hematite pathway; furthermore, comparing data from different Holocene soils formed under various climatic conditions, Torrent et al. (2010 and references therein) also found a relationship between the hematite/maghemite ratio and mean annual temperatures, whereby the higher (lower) the temperature, the higher (lower) the formation of hematite relative to maghemite.

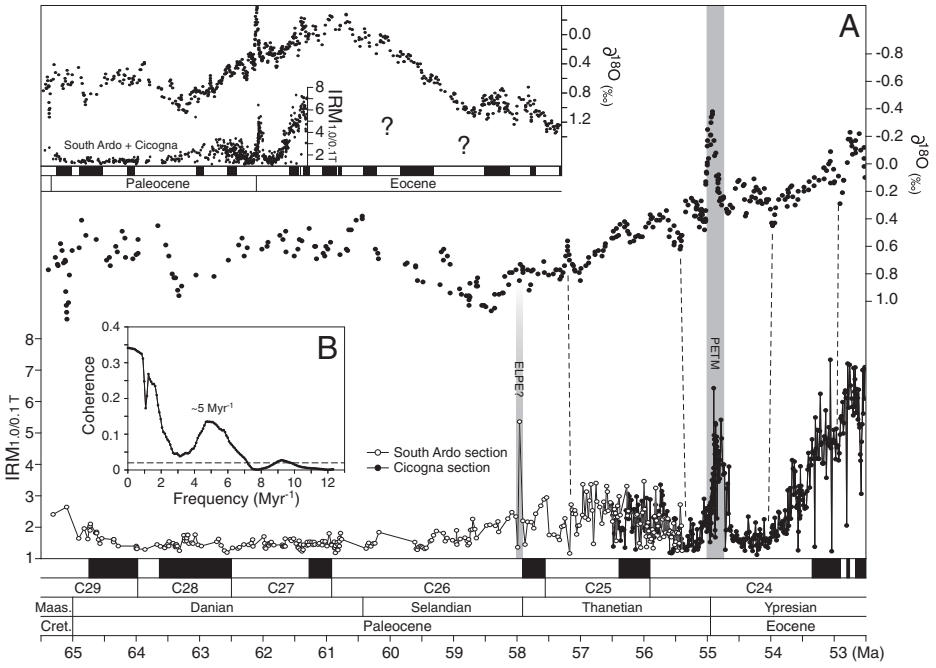

Fig. 9. (A) The Paleocene–early Eocene composite $IRM_{1.0/0.1T}$ dataset from South Ardo (this study) and Cicogna (Dallanave et al., 2010) is compared with the $\delta^{18}O$ climate proxy record of Zachos et al. (2001). Both time series are placed onto a common CK95 time scale, with the K/Pg boundary placed at 65 Ma (Cande and Kent, 1995), and the Paleocene–Eocene boundary at 54.95 Ma following Zachos et al. (2001). (B) Coherence spectrum between the composite $IRM_{1.0/0.1T}$ curve and the $\delta^{18}O$ record. The dashed line represents the 95% level of confidence. See text for discussion.

To evaluate the reliability of our correlation between the Paleocene–Eocene $IRM_{1.0/0.1T}$ record and the benthic $\delta^{18}O$ climate proxy record, we used the coherence function, which is a measure by which two signals may be compared quantitatively in the frequency domain. We applied the coherence function on two new $IRM_{1.0/0.1T}$ and $\delta^{18}O$ series equally spaced in time, generated after calculating the additive inverse of the $\delta^{18}O$ time series. The plot of the squared coherence indicates the range of frequencies for which the two time series are coherent (Fig. 9B); we calculated a value of 0.02 as the minimum coherence at 95% confidence level using the relation given by Chave and Filloux (1985). The two time series are generally coherent over a range of frequencies between 0 and ~7 Myr^{-1}, with a relative minimum spike observed corresponding to a wavelength of ~1 Myr (i.e. frequency = 1.07 Myr^{-1}). The maximum level of coherence is observed at 0 and ~5 Myr^{-1}, implying a good correlation respectively along the entire length of the series and along a wavelength of ~200 kyr, which is approximately the duration of the prominent $IRM_{1.0/0.1T}$ excursion occurring during the PETM.

9. Conclusion

The calcareous nannofossil biostratigraphy and magnetostratigraphy of the South Ardo section indicate that the section spans from the *Micula murus Zone* to the NP10 Zone, and from Chrons C29r to C24r. A continuous and expanded late Cretaceous to early Eocene record is thus documented and serves to improve and refine the calcareous nannofossil biostratigraphy and biochronology of this interval. The rock-magnetic data from the South Ardo section integrated with previously published data from the Eocene Cicogna section (Dallanave et al., 2010) confirm and further substantiate the model proposed in Dallanave et al. (2010) of climate forcing on type and relative amounts of Fe-oxides deposited as detrital phases in the Belluno Basin. During the relatively cool climate of the Paleocene, when the South Ardo sediments deposited, we observe low relative concentration of detrital hematite, saved possibly for the short-lived ELPE warming event characterized by a somewhat higher hematite content; the formation, transport, and deposition of detrital hematite were instead markedly promoted during periods of enhanced chemical weathering rates, which are typical of the warm and humid climates of the PETM and the EECO. This first-order correlation between rock-magnetism and climate is in agreement with the negative feedback mechanism to buffer the Earth's surface temperature variations first proposed by Walker et al. (1981). This model predicts that the CO_2 released in the atmosphere–ocean reservoir by volcanic and metamorphic activity is transferred to the lithosphere through the weathering of silicates followed by marine carbonates sedimentation. A rise in atmospheric pCO_2 causes an increase in mean surface temperatures by the greenhouse effect, which promotes the efficiency of CO_2-consuming chemical weathering processes of silicate rocks on land (most efficiently the basalts; Dessert et al., 2003), with the final result to counterbalance the initial CO_2 rise and prevent runaway greenhouse climates. This long-term negative feedback control of the pCO_2 variations has been the climate stabilizing mechanism over Earth's history during the Phanerozoic (Walker et al., 1981; Gibbs et al., 1999; Kump et al., 2000), and it left its marks in the Paleocene–Eocene sediments of the Belluno Basin, which contains detrital magnetic phases with different oxidation states (hematite vs. magnetite–maghemite) depending on the intensity of the chemical weathering on land.

Supplementary data to this article can be found online at http://dx.doi.org/10.1016/j.palaeo.2012.04.007.

Acknowledgments

We would like to thank E. Fornaciari and L. Giusberti for fruitful discussions and assistance in the field. ED, CA and DR were supported by the University of Padova. We thank three anonymous reviewers for comments that greatly improved this manuscript.

References

Agnini, C., Fornaciari, E., Giusberti, L., Backman, J., Capraro, L., Grandesso, P., Luciani, V., Muttoni, G., Rio, D., Tateo, F., 2005. The Early Paleogene of the Valbelluna (Venetian Southern Alps). Fieldtrip Guidebook ODP Leg 208 Post-Cruise Meeeting. Cooperativa Libraria Editrice Università di Padova (CLEUP), Padova. 32 pp.

Agnini, C., Muttoni, G., Kent, D.V., Rio, D., 2006. Eocene biostratigraphy and magnetic stratigraphy from Possagno, Italy: the calcareous nannofossils response to climate variability. Earth and Planetary Science Letters 241, 815–830.

Agnini, C., Fornaciari, E., Raffi, I., Rio, D., Röhl, U., Westerhold, T., 2007a. High-resolution nannofossil biochronology of middle Paleocene to early Eocene at ODP Site 1262: implications for calcareous nannoplankton evolution. Marine Micropaleontology 64, 215–248.

Agnini, C., Fornaciari, E., Rio, D., Tateo, F., Backman, J., Giusberti, L., 2007b. Responses of calcareous nannofossils assemblages, mineralogy and geochemistry to the environmental perturbations cross the Paleocene/Eocene boundary in the Venetian Pre-Alps. Marine Micropaleontology 63, 19–38.

Agnini, C., Dallanave, E., Fornaciari, E., Giusberti, L., Grandesso, P., Rio, D., Backman, J., Capraro, L., Lanci, L., Luciani, V., Muttoni, G., Pälike, H., Spofforth, D., Tateo, F., 2008. Il Paleogene inferiore in facies pelagica del Veneto nord-orientale. Rendiconti Online - Società Geologica Italiana 4, 5–12.

Agnini, C., Macrì, P., Backman, J., Brinkhuis, H., Fornaciari, E., Giusberti, L., Luciani, V., Rio, D., Sluijs, A., Speranza, F., 2009. An early Eocene carbon cycle perturbation at ~52.5 Ma in the Southern Alps: chronology and biotic response. Paleoceanography 24, PA2209. http://dx.doi.org/10.1029/2008PA001649.

Agnini, C., Forniaciari, E., Giusberti, L., Grandesso, P., Lanci, L., Luciani, V., Muttoni, G., Pälike, H., Rio, D., Spofforth, D.J.A., Stefani, C., 2011. Integrated biomagnetostratigraphy of the Alano section (NE Italy): a proposal for defining the middle-late Eocene boundary. Geological Society of America Bulletin 123, 841–872.

Aubry, M.-P., 1995. From chronology to stratigraphy: interpreting the Lower and Middle Eocene stratigraphic record in the Atlantic Ocean. In: Berggren, W.A., et al. (Ed.), Geochronology, Time Scales and Global Stratigraphic Correlation: Soc. for Sediment. Geol. Tulsa, Okla., Spec. Publ., 54, pp. 213–274.

Backman, J., Shackleton, N.J., 1983. Quantitative biochronology of Pliocene and early Pleistocene calcareous nannoplankton from the Atlantic, Indian and Pacific Oceans. Marine Micropaleontology 8, 141–170. http://dx.doi.org/10.1016/0377-8398(83)90009-9.

Berggren, W.A., Kent, D.V., Swisher III, C.C., Aubry, M.-P., 1995. A revised Cenozoic geochronology and chronostratigraphy. In: Berggren, W.A., et al. (Ed.), Geochronology, Time Scales and Global Stratigraphy Correlation: Soc. for Sediment. Geol., Tulsa, Okla., Spec. Publ., 54, pp. 129–213.

Bernaola, G., Baceta, J.I., Orue-Etxebarria, X., Alegret, L., Maite -Rubio, M., Arostegui, J., Dinarès-Turell, J., 2007. Evidence of an abrupt environmental disruption during the mid-Paleocene biotic event (Zumaia section, western Pyrenees). Geological Society of America Bulletin 119 (7), 785–795. http://dx.doi.org/10.1130/B26132.1.

Besse, J., Courtillot, V., 2002. Apparent and true polar wander and the geometry of the geomagnetic field over the last 200 Myr. Journal of Geophysical Research 107 (B11), 2300. http://dx.doi.org/10.1029/2000JB000050.

Besse, J., Courtillot, V., 2003. Correction to "Apparent and true polar wander and the geometry of the geomagnetic field over the last 200 Myr". Journal of Geophysical Research 108 (B10), 2469. http://dx.doi.org/10.1029/2003JB002684.

Bowles, J., 2006. Data report: revised magnetostratigraphy and magnetic mineralogy of sediments from Walvis Ridge, Leg 208. In: Kroon, D., Zachos, J.C., Richter, C. (Eds.), Proc. ODP, Sci. Results, 208. Ocean Drilling Program, College Station, TX, pp. 1–24.

Bukry, D., Bramlette, M.N., 1970. Coccolith age determinations Leg 3, Deep Sea Drilling Project. In: Maxwell, A.E., et al. (Ed.), Initial Reports of the Deep Sea Drilling Project, vol. 3. U.S. Government Printing Office, Washington, D.C., pp. x589–x611.

Cande, S.C., Kent, D.V., 1992. A new geomagnetic polarity time scale for the Late Cretaceous and Cenozoic. Journal of Geophysical Research 97, 13917–13951.

Cande, S.C., Kent, D.V., 1995. Revised calibration of the geomagnetic polarity time scale for the Late Cretaceous and Cenozoic. Journal of Geophysical Research 100 (B4), 6093–6096. http://dx.doi.org/10.1029/94JB03098.

Castellarin, A., Cantelli, L., 2000. Neo-Alpine evolution of the Southern Eastern Alps. Journal of Geodynamics 30, 251–274.

Chave, A.D., Filloux, J.H., 1985. Observation and interpretation of the seafloor vertical electric field in the Eastern North Pacific. Geophysical Research Letters 12, 793–796.

Cogné, J.P., 2003. PaleoMac: a Macintosh™ application for treating paleomagnetic data and making plate reconstructions. Geochemistry, Geophysics, Geosystems 4 (1), 1007. http://dx.doi.org/10.1029/2001GC000227.

Costa, V., Doglioni, C., Grandesso, P., Masetti, D., Pellegrini, G.B., Tracanella, E., 1996. Carta Geologica d'Italia, Foglio 063, Belluno. Roma, Servizio Geologico d'Italia, scale 1:50,000. 1 sheet + 74 p.

Cramer, B.S., Wright, J.D., Kent, D.V., Aubry, M.-P., 2003. Orbital climate forcing of d13C excursions in the late Paleocene – early Eocene (chrons C24n–C25n). Paleoceanography 18 (4), 1097. http://dx.doi.org/10.1029/2003PA000909.

Dallanave, E., Agnini, C., Muttoni, G., Rio, D., 2009. Magneto-biostratigraphy of the Cicogna section (Italy): implications for the late Paleocene–early Eocene time scale. Earth and Planetary Science Letters 285, 39–51. http://dx.doi.org/10.1016/j.epsl.2009.05.033.

Dallanave, E., Tauxe, L., Muttoni, G., Rio, D., 2010. Silicate weathering machine at work: rock magnetic data from the late Paleocene–early Eocene Cicogna section, Italy. Geochemistry, Geophysics, Geosystems 11 (7), Q07008. http://dx.doi.org/10.1029/2010GC003142.

Dessert, C., Dupre, B., Gaillarde, J., Francois, L.M., Allegre, C.J., 2003. Basalt weathering laws and the impact of basalt weathering on the global carbon cycle. Chemical Geology 202, 257–273.

Di Napoli Alliata, E., Proto Decima, F., Pellegrini, G.B., 1970. Studio Geologico, Stratigrafico e Micropaleontologico dei Dintorni di Belluno. Memorie della Società Geologica Italiana 9, 1–28.

Dinarès-Turell, J., Baceta, J.I., Pujalte, V., Orue-Etxebarria, X., Bernaola, G., 2002. Magnetostratigraphic and cyclostratigraphic calibration of a prospective Paleocene/Eocene stratotype at Zumaia (Basque Basin, Northern Spain). Terra Nova 14, 371–378.

Dinarès-Turell, J., Baceta, J.I., Pujalte, V., Orue-Etxebarria, X., Bernaola, G., Lorito, S., 2003. Untangling the Paleocene climatic rhythm: an astronomically calibrated Early Paleocene magnetostratigraphy and biostratigraphy at Zumaia (Basque Basin, Northern Spain). Earth and Planetary Science Letters 216, 483–500.

Dinarès-Turell, J., Baceta, J.I., Bernaola, G., Orue-Etxebarria, X., Pujalte, V., 2007. Closing the Mid-Paleocene gap: toward a complete astronomically tuned Paleocene Epoch and Selandian and Thanetian GSSPs at Zumaia (Basque Basin, W Pyrenees). Earth and Planetary Science Letters 262, 450–467.

Fisher, R.A., 1953. Dispersion on a sphere. Proceedings of the Royal Society of London A217, 295–305.

Fornaciari, E., Giusberti, L., Luciani, L., Tateo, F., Agnini, C., Backman, J., Oddone, M., Rio, D., 2007. An expanded Cretaceous–Tertiary transition in a pelagic setting of the Southern Alps (central-western Tethys). Palaeogeography, Palaeoclimatology, Palaeoecology 255, 98–131.

Gibbs, M.T., Bluth, G.J.S., Fawcett, P.J., Kump, L.R., 1999. Global chemical erosion over the last 250 My: variations due to changes in paleogeography, paleoclimate, and paleoecology. American Journal of Science 299, 611–651.

Giusberti, L., Rio, D., Agnini, C., Backman, J., Fornaciari, E., Tateo, F., Oddone, M., 2007. Mode and tempo of the Paleocene-Eocene thermal maximum in an expanded section from the Venetian pre-Alps. Geological Society of America Bulletin 119, 391–412. http://dx.doi.org/10.1130/B25994.1.

Jiang, M.J., Gartner, S., 1986. Calcareous nannofossil succession across the Cretaceous/Tertiary boundary in east-central Texas. Micropaleontology 32, 232–254.

Kent, D.V., Tauxe, L., 2005. Corrected Late Triassic latitudes for continents adjacent to the North Atlantic. Science 307, 240–244.

Kent, D.V., Olsen, P.E., Witte, W.K., 1995. Late Triassic–earliest Jurassic geomagnetic polarity sequence and paleolatitudes from drill cores in the Newark rift basin, eastern North America. Journal of Geophysical Research 100, 14965–14998.

King, R.F., 1955. The remanent magnetism of artificially deposited sediments. Monthly Notices of the Royal Astronomical Society: Geophysical Supplement 7, 115–134.

Kirschvink, J.L., 1980. The least-squares line and plane and analysis of paleomagnetic data. Geophysical Journal of the Royal Astronomical Society 62, 699–718.

Kruiver, P.P., Dekkers, M.J., Heslop, D., 2001. Quantification of magnetic coercivity components by the analysis of acquisition curves of isothermal remanent magnetization. Earth and Planetary Science Letters 189, 269–276.

Kump, L.R., Brantley, S.L., Arthur, M.A., 2000. Chemical weathering, atmospheric CO_2, and climate. Annual Review of Earth and Planetary Sciences 28, 611–667.

Lowrie, W., 1990. Identification of ferromagnetic minerals in a rock by coercivity and unblocking temperature properties. Geophysical Research Letters 17, 150–162.

Lowrie, W., Alvarez, W., 1977. Upper Cretaceous–Paleocene magnetic stratigraphy at Gubbio, Italy: III. Upper Cretaceous magnetic stratigraphy. Geological Society of America Bulletin 88, 374–377.

Lowrie, W., Alvarez, W., Napoleone, G., Perch-Nielsen, K., Premoli Silva, I., Toumarkine, M., 1982. Paleogene magnetic stratigraphy in Umbrian pelagic carbonate rocks: the Contessa sections, Gubbio. Geological Society of America Bulletin 93, 414–432.

Martini, E., 1971. Standard Tertiary and Quaternary calcareous nannoplankton zonation. In: Farinacci, A. (Ed.), Proceedings of the 2nd Planktonic Conference, 2. Tecnoscienza, Roma, pp. 739–785.

McFadden, P.L., McElhinny, M.W., 1990. Classification of the reversal test in palaeomagnetism. Geophysical Journal International 103, 725–729.

Monechi, S., Thierstein, H.R., 1985. Late Cretaceous–Eocene nannofossil and magnetostratigraphic correlations near Gubbio, Italy. Marine Micropaleontology 9, 419–440.

Ogg, J.G., Smith, A.G., 2004. The geomagnetic polarity time scale. In: Gradstein, F.M., Ogg, J.G., Smith, A.G. (Eds.), A Geological Time Scale, 2004. Cambridge University Press, Cambridge, UK. 589 p.

Okada, H., Bukry, D., 1980. Supplementary modification and introduction of code numbers to the low-latitude coccolith biostratigraphic zonation (Bukry, 1973; 1975). Marine Micropaleontology 5, 321–325.

Perch-Nielsen, K., 1981. Nouvelles observations sur les nannofossiles calcaires à la limite Crétacé/Tertiare près de El Kef (Tunisie). Cahiers de Micropaléontologie 3, 25–36.

Perch-Nielsen, K., 1985a. Mesozoic calcareous nannofossils. In: Bolli, H.M., et al. (Ed.), Plankton Stratigraphy. Cambridge University Press, New York, pp. 329–426.

Perch-Nielsen, K., 1985b. Cenozoic calcareous nannofossils. In: Bolli, H.M., et al. (Ed.), Plankton Stratigraphy. Cambridge University Press, New York, pp. 427–554.

Petrizzo, M.R., 2005. An Early Late Paleocene Event on Shatsky Rise, Northwest Pacific Ocean (ODP Leg 198): evidence from Planktonic Foraminiferal Assemblages. In: Bralower, T.J., Premoli Silva, I., Malone, M.J. (Eds.), Proc. ODP, Sci. Results, 198Proc. Ocean Drill. Program, Sci. Results, 198, pp. 1–29. http://dx.doi.org/10.2973/odp.proc.sr.198.102.2005.

Raffi, I., Backman, J., Pälike, H., 2005. Changes in calcareous nannofossil assemblage across the Paleocene/Eocene transition from the paleo-equatorial Pacific Ocean. Palaeogeography, Palaeoclimatology, Palaeoecology 226, 93–126.

Raffi, I., Backman, J., Fornaciari, E., Pälike, H., Rio, D., Lourens, L.J., Hilgen, F.J., 2006. A review of calcareous nannofossil astrobiochronology encompassing the past 25 million years. Quaternary Science Reviews 25, 3113–3137. http://dx.doi.org/10.1016/j.quascirev.2006.07.007.

Romein, A.J.T., 1979. Lineages in early Paleogene calcareous nannoplankton. Utrecht Micropaleontological Bulletins 22 231 pp.

Spofforth, D.J.A., Agnini, C., Pälike, H., Rio, D., Bohaty, S., Fornaciari, E., Giusberti, L., Lanci, V., Luciani, V., Muttoni, G., 2010. Organic carbon burial following the middle Eocene climatic optimum (MECO) in the central-western Thethys. Paleoceanography 25, PA3210. http://dx.doi.org/10.1029/20091738.

Tauxe, L., 2005. Inclination flattening and the geocentric axial dipole hypothesis. Earth and Planetary Science Letters 233, 247–261.

Tauxe, L., 2010. Essentials of Paleomagnetism. Univ. California Press, Berkeley.

Tauxe, L., Kent, D.V., 1984. Properties of detrital remanence carried by hematite from study of modern river deposits and laboratory redeposition experiments. Geophysical Journal of the Royal Astronomical Society 76, 543–561.

Tauxe, L., Kent, D.V., 2004. A simplified statistical model for the geomagnetic field and the detection of shallow bias in paleomagnetic inclinations: was the ancient magnetic field dipolar?. edited by In: Channell, J.E.T., Kent, D.V., Lowrie, W., Meert, J.G. (Eds.), Timescales of the Paleomagnetic Field. : AGU monograph, 145. AGU, Washington, DC.

Tauxe, L., Kodama, K.P., Kent, D.V., 2008. Testing for paleomagnetic inclination error in sedimentary rocks: a comparative approach. Physics of the Earth and Planetary Interiors 169, 152–165.

Torrent, J., Barrón, V., Liu, Q.S., 2006. Magnetic enhancement is linked to and precedes hematite formation in aerobic soil. Geophysical Research Letters 33, L02401. http://dx.doi.org/10.1029/2005GL024818.

Torrent, J., Liu, Q.S., Barrón, V., 2010. Magnetic susceptibility changes in relation to pedogenesis in a Xeralf chronosequence in northwestern Spain. European Journal of Soil Science 61, 161–173. http://dx.doi.org/10.1111/j.1365-2389.2009.01216.x.

Van Heck, S.E., Prins, B., 1987. A refined nannoplankton zonation for the Danian of the Central North Sea. Abhandlungen der Geologischen Bundesanstalt (Austria) 39, 285–303.

Walker, J.C.G., Hays, P.B., Kasting, J.F., 1981. A negative feedback mechanism for the long-term stabilization of the Earth's surfaces temperature. Journal of Geophysical Research 86, 9776–9782.

Watson, G., 1983. Large sample theory of the Langevin distributions. Journal of Statistical Planning and Inference 8, 245–256.

Westerhold, T., Röhl, U., 2006. Data report: revised composite records for Shatsky Rise Sites 1209, 1210, and 1211. In: Bralower, T.J., Primoli-Silva, I., Malone, M.J. (Eds.), Proc. ODP, Sci. Results, 198. Ocean Drilling Program, College Station, TX, pp. 1–26. http://dx.doi.org/10.2973/odp.proc.sr.198.122.2006.

Westerhold, T., Röhl, U., Raffi, I., Fornaciari, E., Monechi, S., Reale, V., Bowles, J., Evans, H.F., 2008. Astronomical calibration of the Paleocene time. Palaeogeography, Palaeoclimatology, Palaeoecology 257, 377–403.

Winterer, E.L., Bosellini, A., 1981. Subsidence and sedimentation on Jurassic passive continental margin, Southern Alps, Italy. AAPG Bulletin 65, 394–421.

Zachos, J., Pagani, M., Sloan, L., Thomas, E., Billups, K., 2001. Trends, rhythms and aberrations in global climate 65 Ma to present. Science 292, 686–693.

Zachos, J.C., Kroon, D., Blum, P., et al., 2004. Proc. ODP, Init. Repts, 208. Ocean Drilling Program, College Station, TX. http://dx.doi.org/10.2973/odp.proc.ir.208.2004.

Zijderveld, J.D.A., 1967. A.C. demagnetization of rocks: analysis of results. In: Collinson, D.W., et al. (Ed.), Methods in Paleomagnetism. Elsevier, Amsterdam, pp. 254–286.